Probabilistic description of short-term cloud dynamics from rapid sampling of the solar spectral irradiance

Anderson, Nick, Tatsiankou, Viktar, Hinzer, Karin, Beal, Richard, Schriemer, Henry

Nick Anderson, Viktar Tatsiankou, Karin Hinzer, Richard Beal, Henry Schriemer, "Probabilistic description of short-term cloud dynamics from rapid sampling of the solar spectral irradiance," Proc. SPIE 11996, Physics, Simulation, and Photonic Engineering of Photovoltaic Devices XI, 119960B (4 March 2022); doi: 10.1117/12.2616231

SPIE.

Event: SPIE OPTO, 2022, San Francisco, California, United States

Probabilistic Description of Short-Term Cloud Dynamics from Rapid Sampling of the Solar Spectral Irradiance

Nick Anderson[a], Viktar Tatsiankou[a,b], Karin Hinzer[a], Richard Beal[b], Henry Schriemer*[a]
[a]SUNLAB, University of Ottawa, 800 King Edward Ave, Ottawa, ON, CAN, K1N 6N5
[b]Spectrafy, 4 Florence St, #204, Ottawa, ON, CAN, K2P 0W7

ABSTRACT

Solar irradiance variability due to stochastic cloud dynamics can cause unwanted fluctuations in the output voltage of photovoltaic (PV) modules. These dynamics must in particular be understood at very-short and short time scales if grid interconnection and generation/load balance requirements are to be maintained for PV distributed across the grid edge. Using a recently-created database for Ottawa, Canada, a 6-month longitudinal study was conducted with a specific focus on cloud dynamics. A spectral pyranometer was used to derive full-range spectral and broadband global horizontal irradiance under all sky conditions every 250 ms. Exploiting the infrared (IR) measurement channel of this software-augmented multi-filter radiometer allowed the cloud dynamics to be probed across time scales ranging from the sub-second to ~30 minutes. Seven distinct sky conditions were self-consistently determined without sky imaging. Probability distributions, established via kernel density estimates (KDE), allowed the statistical dependence of these conditions on the spectral clear-sky index to be found. The stochastic nature of the spectral irradiance variability was probed using spectral clear-sky index increments, over time steps that were found to span three distinct variability regimes.

Keywords: Solar irradiance variability, cloud dynamics, spectral pyranometer, probability density, index increments

1. INTRODUCTION

Photovoltaics (PV) is a key enabler of the global energy transformation.[1, 2] Within the emerging smart grid context,[3] this sustainable generation technology may be regionally capable of supporting the entire electrical load with a high penetration of distributed PV fleets if one follows a firm forecast overbuild/curtail/storage strategy to address the intermittent nature of the solar resource.[4] In this strategy, the short-term forecast uncertainty associated with weather-driven solar irradiance fluctuations is reduced by exploiting geographic dispersion to realize firm power generation. However, for PV systems as distributed energy resources (DER) at the edge of the distribution grid, the interconnection constraints[5] require "nodal approaches for the computation of power grid congestion constraints and power flow solutions".[6] To facilitate the energy transition, effective DER participation in local energy markets must be addressed as a fully transactive energy system under uncertainty.[7] For many grid services, in both settlement and control, this requires intra-hour forecasting (also known as "nowcasting"), which ranges from a few seconds to an hour and encompasses very-short-term and short-term categories.[8] A recent review has focused on the often neglected temporal and spatial resolution aspects of solar irradiance and power forecasting methods,[9] but it is safe to say that probabilistic solar forecasting capabilities are still immature.[10]

Maturation of probabilistic solar forecasting is a process that requires advances in instrumentation, accessibility to data, application, and assessment. A definitive approach to solar forecasting research practice "intended to facilitate comparison, comprehension, and communication within the solar forecasting field, and [to] speed up its development",[11] is the "ROPES" guideline (which stands for reproducible, operational, probabilistic/physical, ensemble, and skill) proposed by Dazhi Yang. We take this formalism as our goal for an operational implementation of PV generation nowcasting at the grid edge. Here we address its enabling requirements with an instrumentation and data analysis focus, employing a new spectral irradiation database for Ottawa, Canada. This database provides an ongoing comprehensive meteorological and solar spectral irradiance record, with measurements every 250 ms, beginning 1 June 2021 and here ending 30 November 2021. We describe the novel spectral pyranometer that acquired this data, and which enables the

*hschriemer@uottawa.ca

Physics, Simulation, and Photonic Engineering of Photovoltaic Devices XI, edited by Alexandre Freundlich, Stéphane Collin, Karin Hinzer, Proc. of SPIE Vol. 11996, 119960B · © 2022 SPIE · 0277-786X · doi: 10.1117/12.2616231

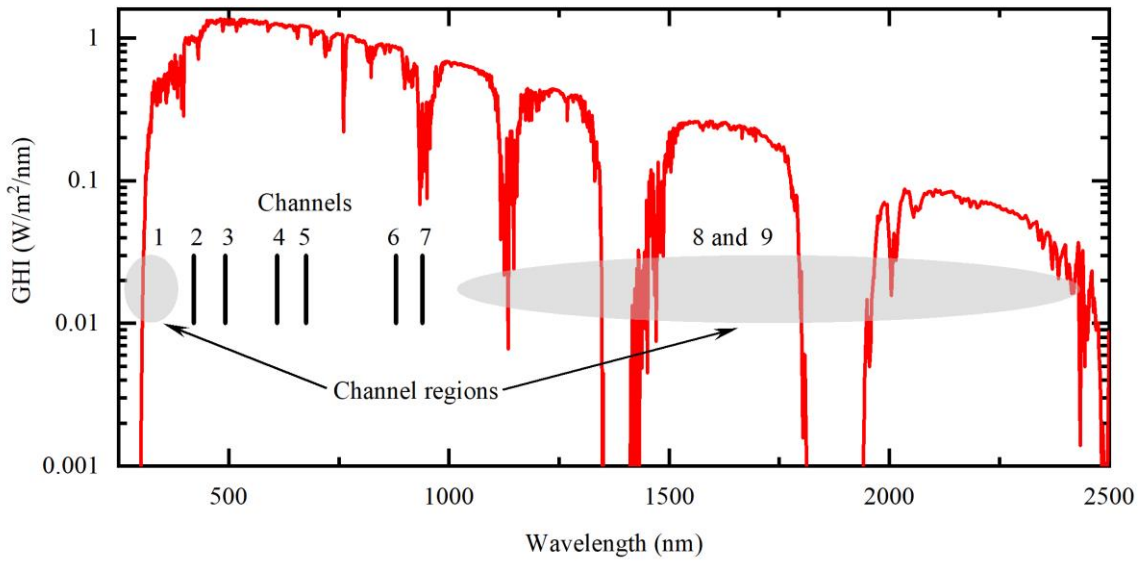

Figure 1. Spectral irradiance at 1:03 pm on 3 August 2021; the wavelength range from 2500 to 4000 nm is not shown. The measurement channel locations are as indicated. The precise locations of channels 1, 8 and 9 are not given for proprietary reasons.

ongoing self-consistent determination of sky conditions. Our preliminary data analysis first addresses the distribution of sky conditions over this 6-month period, and then statistically describes cloud dynamics as a function of clear-sky index increments for time scales less than 10 minutes.

2. INSTRUMENTATION AND SKY CLASSIFICATION

The spectral pyranometer employed in this work is a customized version of Spectrafy's SolarSIM-G, whose general properties have been described elsewhere.[12] It is a software-augmented multi-filter radiometer that measures the spectral global horizontal irradiance (GHI) using narrow bandpass filters paired with calibrated photodetectors. A multiplexer sequentially selects the voltage signal from each spectral channel and feeds it to an analog-to-digital converter sampling at 60 Hz, which is sufficient to accurately capture the fastest of transients.[13] The nine wavelength channels are illustrated in Figure 1 with respect to the spectral GHI for Ottawa at 1:03 pm on 3 August 2021; for proprietary reasons, the locations of the ultraviolet (UV) and infrared (IR) channels cannot be precisely disclosed. In combination with measurements of ambient pressure, relative humidity, and air temperature, this information is employed by a radiative transfer model to self-consistently derive atmospheric optical parameters for the reconstruction in real-time of spectral GHI from 280 nm to 4000 nm. The basic design principles have been previously described.[14] Measurements from the infrared channels are used to classify the clouds by their water morphology, with a uniform cloud model employed to estimate cloud optical depth and to subsequently compute cloud transmittance in the 1000-4000 nm range. The efficacy of this approach has been validated against reference instruments under a full range of sky conditions.[15]

3. RESULTS AND ANALYSES

3.1 The clear-sky index

Denoting the spectral GHI time series measured at wavelength channel λ by $E(\lambda;t)$, the clear-sky spectrum $E_{clr}(\lambda;t)$ is determined as part of the spectral reconstruction process and derives from the same set of underlying atmospheric optical parameters as the actual spectrum, but without the correction for clouds. This self-consistent determination allows the sky condition to be accurately modeled by a spectral clear-sky index

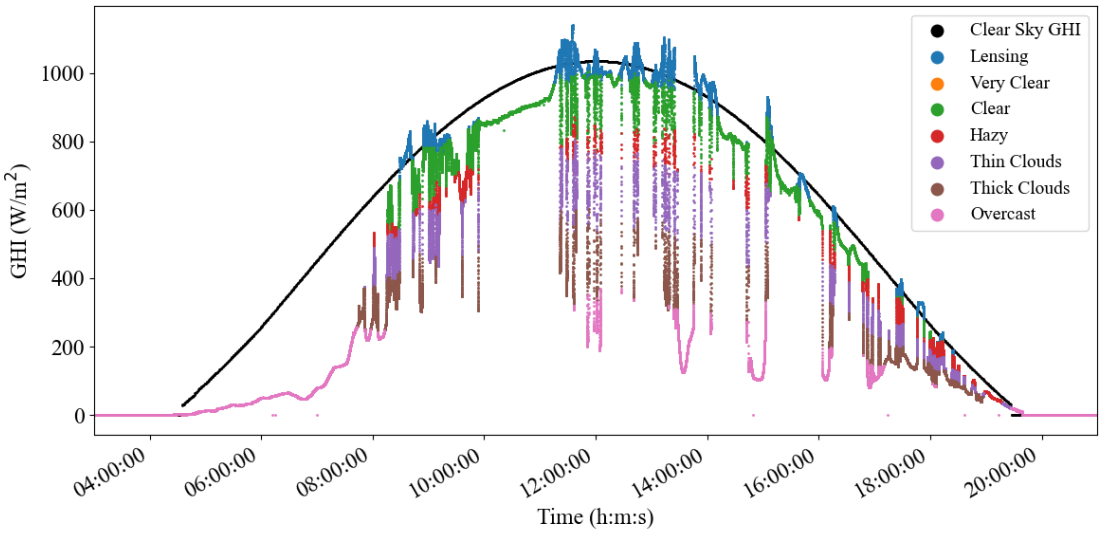

Figure 2. The GHI observed on 1 June 2021 in Ottawa, Canada, color coded for sky condition; the smooth black curve is the GHI that would be observed under clear sky conditions.

$$\kappa^*(\lambda;t) = E(\lambda;t)/E_{clr}(\lambda;t) \tag{1}$$

because seasonal and diurnal effect are now removed. We have elsewhere described the self-consistent classification of sky conditions based on this clear-sky index as part of the decomposition algorithm for deriving the broadband direct normal (DNI) and diffuse horizontal (DHI) irradiances from the spectral GHI.[15] Seven distinct sky conditions are then identified via clear-sky index ranges for measurement channels 1 and 9, as noted in Table 1. Figure 2 presents the broadband GHI observed on 1 June 2021, color coded for sky condition; the smooth black curve is the GHI that would be observed under equivalent clear sky conditions. Note that the clear-sky index is $k^*(t) = \mathrm{GHI}(t)/\mathrm{GHI}_{clr}(t)$, which is the broadband version of equation (1). Our focus, however, will be on the spectral clear-sky index.

Table 1. Classification of sky conditions based on channels 1 and 9.[15]

Sky condition	**$\kappa^*(\lambda_1)$**		**$\kappa^*(\lambda_9)$**	
	Min	*Max*	*Min*	*Max*
Lensing	–	–	1.05	–
Very clear	1.0	–	0.75	1.05
Clear	0.8	1.0	0.75	1.05
Hazy	–	0.8	0.75	1.05
Thin clouds			0.5	0.75
Thick clouds			0.25	0.5
Overcast			–	0.25

3.2 Distribution of sky conditions

The probability distributions for all sky conditions were determined by kernel density estimation (KDE); the data of channel 9 were used as this channel is the primary metric for sky classification. The results are shown in Figure 3 as a plot of probability densities versus clear-sky indices. The black curve shows the density for the sum total of all sky conditions, while the colored curves show those for the individual sky conditions. This enables us to visualize the

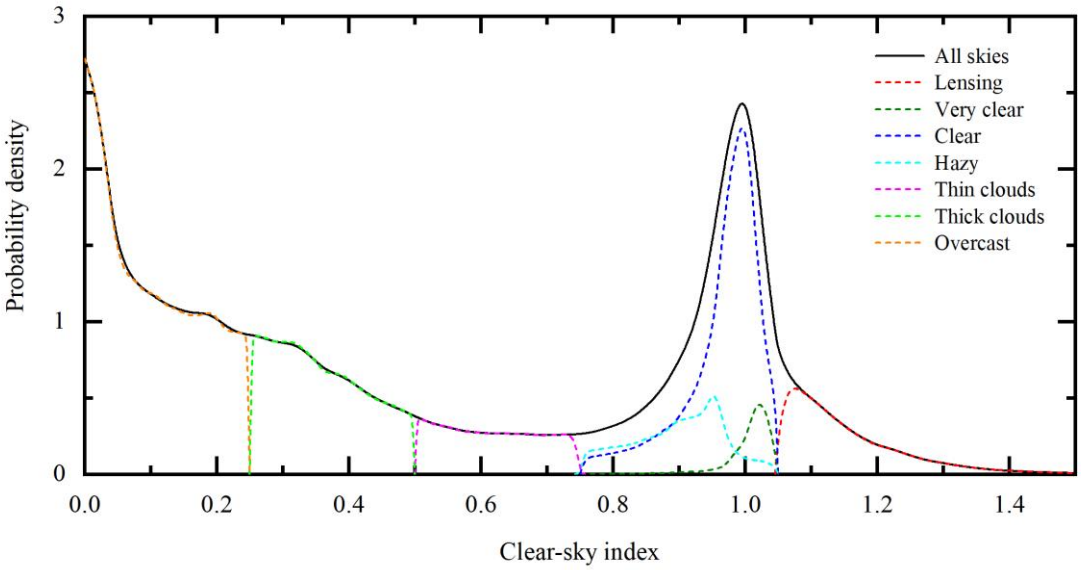

Figure 3. Statistical dependence of sky condition on spectral (channel 9) clear-sky index; the black curve gives the probability density for all sky conditions while the colored curves show those for the individual sky conditions, as labeled.

relative time spent in each cloud state. As described in Table 1, the thin, thick, and overcast distributions are independent of one another, while hazy, clear and very clear distributions overlap but with distinctly different dependencies on spectral clear-sky index.

3.3 Irradiance variability

We quantify irradiance variability using increments in the spectral clear sky index as

$$\Delta\kappa_\tau^*(\lambda;t) = \kappa^*(\lambda;t+\tau) - \kappa^*(\lambda;t), \tag{2}$$

where τ refers to the increment time step. The probability distribution of these increments describes the likelihood that sky conditions will persist for the given increment. Thus, for any increment, the probability distribution peaks in the limit as $\Delta\kappa_\tau^* \to 0$; that is, relatively small changes in the clear-sky index have the highest probability, with greater changes tailing off with decreasing probability. Figure 4 shows the dependence of the probability density, determined via kernel density estimates, on index increment for the different measurement channels; Figure 4(a) is for an increment time step of 600 s, while Figure 4(b) is for an increment time step of 1 s; both figures span the same range of densities. For the long time step, which spans the entire range of variability, spectral sensitivity is observed, which is easiest seen at large index increments (note the log scale). However, for the short time step, the spectral sensitivity is about twice as strong, as the variation in peak heights reveal, although only small index increments can be probed. Collectively, these demonstrate the spectral dependence of the probability density, with the IR channel (channel 9 – purple curve) typically spanning the greatest irradiance variability at all time steps.

The probability density is known to narrow as the increment time step is reduced, with the tails becoming more pronounced as the time step is increased.[16] This behavior is illustrated using the channel 9 (IR) spectral clear-sky index for increment time steps ranging from 1 s to 600 s. Channel 9 is chosen so as to be consistent with the sky classification procedure, as it is the channel most sensitive to cloud absorption and scattering.[15] Figure 5(a) shows the monotonic increase of the peak density, and the concomitant narrowing of the distribution, as the time step is decreased. This behavior is quantified in Figure 5(b), where the peak densities and their corresponding full widths at half maximum (FWHM) are plotted as a function of the increment time step; the former is shown on the right axis (blue squares) as a log-log plot, while the latter is shown on the left axis (red circles) as a lin-log plot.

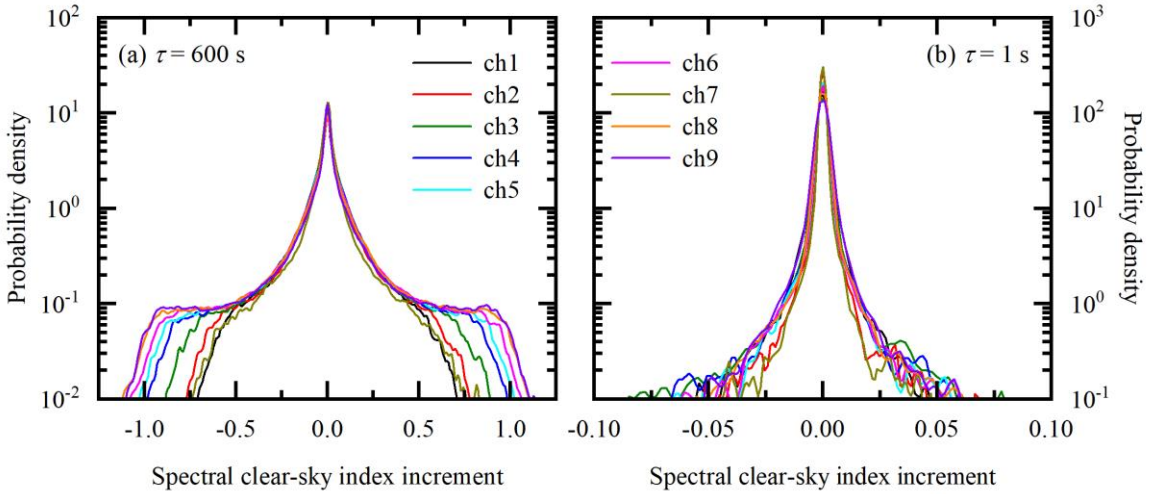

Figure 4. Channel dependence of the probability densities vs spectral clear-sky index increments for (a) a 600-s time step, and (b) a 1-s time step.

The kernel density estimation used to accurately describe the probability densities is a nonparametric method. Given the fat-tailed behavior of these distributions, the FWHM is therefore not expected to provide a definitive signature of the variability.[16] The peak density, however, is well-defined and is a highly sensitive metric. The peak density in Figure 5(b) is seen to increase monotonically with decreasing time step, but clear evidence of power law scaling is shown across three distinct temporal regimes within the ~30-minute variability period studied. Atmospheric variability is known to be dominated by scaling processes[17], and power law scaling has been shown to describe cumulus cloud size distribution.[18] The slope is therefore characteristic of the underlying variability. The short-time high-slope regime is very likely a sign of ramping behavior (i.e., when the sun's disk becomes occluded). A distinct transition happens at ~7 s to a state with reduced variability, which may indicate evolving intra-cloud dynamics. This is followed by a more abrupt transition at about 3 minutes to an intermediate variability state (with a slope between that of the other two), which may be indicative of a long-time regime dominated by transitions from one cloud type to another. The interruption in the monotonic increase in FWHM with increasing time step at this latter transition is consistent with this interpretation.

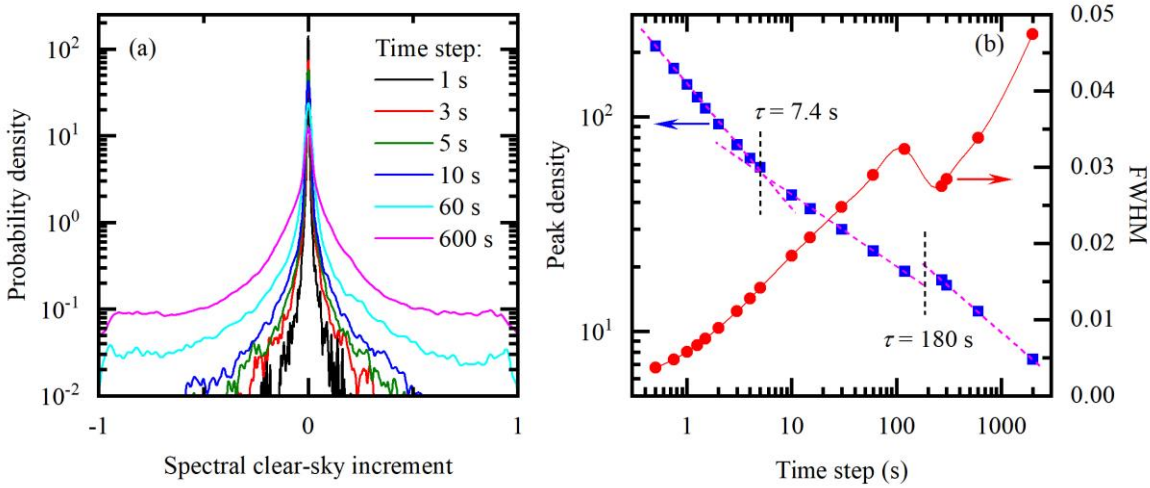

Figure 5. (a) Probability densities vs channel 9 spectral clear-sky index increments for the indicated increment time steps; and (b) their corresponding peak densities and full widths at half maximum (FWHM).

4. CONCLUSIONS

A novel spectral pyranometer was used in the creation of a spectral irradiance database for Ottawa, Canada. A preliminary analysis of the first six months of data, beginning 1 June 2021, from this software-augmented multi-filter radiometer allowed the cloud dynamics to be probed across time scales ranging from the sub-second to ~30 minutes. Sky conditions were self-consistently determined for each time interval without sky imaging. Exploiting the pyranometer's IR measurement channel, the statistical dependence on spectral clear-sky index of these seven distinct sky conditions were established via kernel density estimates of their probability densities. The irradiance variability was quantified using increments in the spectral clear-sky index. The resulting probability densities for a range of time steps spanning sub-second to ~30 minutes were quantified by their peak positions and FWHM. Power law scaling was found across three distinct temporal regimes within this range. They were speculatively associated with ramping behavior, intra-cloud dynamics, and transitions between cloud types. Since the identification of these time scales has implications for the nowcasting of distributed PV resources, further investigation is clearly warranted.

REFERENCES

[1] Gielen, D., Boshell, F., Saygin, D., Bazilian, M.D., Wagner, N., and Gorinia, R., "The role of renewable energy in the global energy transformation," Energy Strategy Reviews 24, 38–50 (2019)

[2] Bogdanov, D., Ram, M., Aghahosseini, A., Gulagi, A., Solomon Oyewo, A., Child, M., Caldera, U., Sadovskaia, K., Farfan, J., De Souza Noel Simas Barbosa, L., Fasihi, M., Khalili, S., Traber, T., and Breyer, C., "Low-cost renewable electricity as the key driver of the global energy transition towards sustainability," Energy 227 (2021)

[3] NIST Framework and Roadmap for Smart Grid Interoperability Standards, Release 3.0, NIST Special Publication 1108r3, National Institute of Standards and Technology (2014)

[4] Perez, R., Perez, M., Schlemmer, J., Dise, J., Hoff, T.E., Swierc, A., Keelin, P., Pierro, M., and Cornaro, C., "From firm solar power forecasts to firm solar power generation an effective path to ultra-high renewable penetration a New York case study," Energies, 13(17):4489, (2020)

[5] IEEE Standards Coordinating Committee 21 on Fuel Cells, Photovoltaics, Dispersed Generation, and Energy Storage, IEEE SStd 1547-2018 - IEEE Standard for Interconnection and Interoperability of Distributed Energy Resources with Associated Electric Power Systems Interfaces, IEEE (2018)

[6] Bachoumis, A., Andriopoulos, N., Plakas, K., Magklaras, A., Alefragis, P., Goulas, G., Birbas, A., and Papalexopoulos, A., "Cloud-edge interoperability for demand response-enabled fast frequency response service provision," IEEE Transactions on Cloud Computing (early access) (2021)

[7] Lezama, F., Soares, J., Hernandez-Leal, P., Kaisers, M., Pinto, T., and Vale, Z., "Local energy markets: paving the path toward fully transactive energy systems," IEEE Transactions on Power Systems, vol. 34, no. 5, pp. 4081-4088 (2019)

[8] Ahmed, R., Sreeram, V., Mishra, Y., and Arif, M.D., "A review and evaluation of the state-of-the-art in PV solar power forecasting: techniques and optimization," Renewable and Sustainable Energy Reviews 124 (2020)

[9] Yang, B., Zhu, T., Cao, P., Guo, Z., Zeng, C., Li, D., Chen, Y., Ye, H., Shao, R., Shu, H., and Yu, T., "Classification and summarization of solar irradiance and power forecasting methods: a thorough review," CSEE Journal of Power and Energy Systems (Early Access) (2021)

[10] Hong, T., Pinson, P., Fan, S., Zareipour, H., Troccoli, A., and Hyndman, R.J., "Probabilistic energy forecasting: Global Energy Forecasting Competition 2014 and beyond," Int J Forecasting 32, 896–913 (2016)

[11] Yang, D., "A guideline to solar forecasting research practice: reproducible, operational, probabilistic or physically-based, ensemble, and skill (ROPES)," J Renew Sustain Ener 11, 022701 (2019)

[12] Tatsiankou, V., Hinzer, K., Schriemer, H., and Beal, R., "Efficient, real-time global spectral and broadband irradiance acquisition," 7th World Conference on Photovoltaic Energy Conversion (2018)

[13] Yordanov, G. H., Saetre, T. O., and Midtgård, O., "Optimal temporal resolution for detailed studies of cloud-enhanced sunlight (overirradiance)," 2013 IEEE 39th Photovoltaic Specialists Conference (PVSC), 0985-0988 (2013)

[14] Tatsiankou, V., Hinzer, K., Schriemer, H., Emery, K., and Beal, R., "Design principles and field performance of a solar spectral irradiance meter," Journal of Solar Energy, vol. 133, 94-102 (2016)

[15] Tatsiankou, V., Hinzer, K., Schriemer, H., and Beal, R., "Improved global irradiance decomposition by sky condition classification from measured spectral clearness indices," 47th IEEE Photovoltaic Specialists Conference (PVSC) (2020)
[16] Lohmann, G.M., "Irradiance variability quantification and small-scale averaging in space and time: a short review," Atmosphere 9, 264-285 (2018)
[17] Lovejoy, S., "Spectra, intermittency, and extremes of weather, macroweather and climate," Sci Rep 8, 12697 (2018)
[18] Neggers, R. A. J., Griewank, P. J., and Heus, T, "Power-law scaling in the internal variability of cumulus cloud size distributions due to subsampling and spatial organization," J Atmos Sci 76, 1489-1503 (2019)